CrossMark

The Simulation of Precipitation Evolutions and Mechanical Properties in Friction Stir Welding with Post-Weld Heat Treatments

Z. Zhang, Z.Y. Wan, L.-E. Lindgren, Z.J. Tan, and X. Zhou

A finite element model of friction stir welding capable of re-meshing is used to simulate the temperature variations. Re-meshing of the finite element model is used to maintain a fine mesh resolving the gradients of the solution. The Kampmann–Wagner numerical model for precipitation is then used to study the relation between *friction stir welds* with post-weld heat treatment (PWHT) and the changes in mechanical properties. Results indicate that the PWHT holding time and PWHT holding temperature need to be optimally designed to obtain FSW with better mechanical properties. Higher precipitate number with lower precipitate sizes gives higher strength in the stirring zone *after PWHT. The coarsening of precipitates in HAZ are the main reason to hinder the improvement of mechanical property when PWHT is used.*

1. Introduction

Friction stir welding (FSW) has been in use for more than 20 years. As a solid-state joining technique, FSW has many advantages compared to fusion welding, like lower defects and distortions, less contaminations, etc. (Ref 1). FSW is suitable for joining aluminum alloys (Ref 2, 3), magnesium alloys (Ref 4-6), titanium alloys (Ref 7, 8), coppers (Ref 9, 10), steels (Ref 11-13), and even dissimilar metals (Ref 14-16). FSW has been applied to automobile, high-speed train, ship, aeronautic, and aerospace industries (Ref 17, 18). Several new technologies building on FSW exist like friction stir processing, friction stir spot welding, etc. Mishra et al. (Ref 19) originally proposed friction stir processing (FSP). FSP was systematically studied by Ma et al. (Ref 20) who found that it caused larger superplasticity.

Several factors are important for controlling FSW qualities. Some aspects are the plastic behavior of the material, the heat generation, and the microstructural evolution. The microstructure after FSW is the most important factor for the controlling the weld quality. It can be affected by the generated heat and the plastic deformation. The Zener–Hollomon parameter is generally used for predictions of grain sizes and grain distributions. Zhang et al. (Ref 21) proposed an effective model with combination of Arbitrary Lagrangian-Eulerian (ALE) model (Ref 22) for prediction of mechanical properties of friction stir welds based on Z-parameter calculations. This method was used in friction stir spot welding (Ref 23) for prediction of grain sizes in an aluminum alloy. It has also been applied to friction stir welding of aluminum, magnesium, titanium, and steel alloys for evaluations of grain sizes and hardness changes (Ref 24-27). The Monte Carlo method is a more accurate method for grain structure calculations and has been systematically used for prediction of grain growth in fusion welding technologies (Ref 28-32). It can be also applied to FSW (Ref 33, 34). The Zener–Hollomon based model (Ref 35) is faster than the Monte Carlo approach.

As mentioned above, microstructural evolution affects mechanical properties of FSW. This also includes precipitate evolution in the case of Al-Mg-Si alloy. A sequentially coupled model, according to Simar et al. (Ref 36), is used to predict the precipitate evolutions in FSW. Genevois et al. (Ref 37) proposed a mixing law for prediction of the yield stress in the welding zones. The precipitate evolution is assumed to be determined by the thermal history, both for the welding and for the following heat treatments, and be connected to the evolution of mechanical properties. Shercliff and Ashby (Ref 38) proposed a semiempirical model based on the classical kinetics theory to describe the changes in yield strength. Myhr and Grong (Ref 39), Shercliff et al. (Ref 40), and Robson et al. (Ref 41) modified this model and applied it for prediction of the hardness distributions in friction stir welds of age hardening of heat-treatable aluminum alloys. This model can be fitted well to predict precipitate evolution of the 2XXX, 6XXX, 7XXX aluminum alloys. However, it can be only applied when the peak-aged state is the initial state due to the assumption that the number density of precipitates is constant. Myhr and Grong (Ref 42) further proposed a new model based on the KWN model (Ref 43) for more accurate description of precipitation in isothermal and non-isothermal states. This model is integrated

Z. Zhang, State Key Laboratory of Structural Analysis for Industrial Equipment, Department of Engineering Mechanics, Faculty of Vehicle Engineering and Mechanics, Dalian University of Technology, Dalian 116024, China and International Research Center for Computational Mechanics, Dalian University of Technology, Dalian 116024, China; Z.Y. Wan, Z.J. Tan, and X. Zhou, State Key Laboratory of Structural Analysis for Industrial Equipment, Department of Engineering Mechanics, Faculty of Vehicle Engineering and Mechanics, Dalian University of Technology, Dalian 116024, China; and L.-E. Lindgren, Luleå University of Technology, 971 87 Luleå, Sweden. Contact e-mail: zhangz@dlut.edu.cn.

into the finite element code as a coupled thermal–metallurgical–mechanical model (Ref 44, 45).

The mechanical properties are usually lower in the SZ than in the base metal for FSW of Al-Mg-Si alloys. They can be recovered by the PWHT (Ref 46-48). Precipitation kinetics of a supersaturated solid solution of Mg in Al-Mg-Si experiences during the aging process as the following steps: SSSS (supersaturated solid solution) → atomic clusters → G.P. zones → β''(Mg$_5$Si$_3$) → β'(Mg$_5$Si$_3$) → β(Mg$_2$Si). Precipitates can grow from smaller β'' to β' in a metastable state. Finally, stable precipitate β can be formed at room temperature. In this process, the evolution of the precipitate distribution plays the key role. The variation of mechanical properties and the formation of residual stresses can affect the final fatigue behavior inside and near the weld, which have been systematically investigated numerically and experimentally (Ref 49-53).

The aim of this work is to develop an integrated model as summarized above in order to be able to describe the FSW and PWHT processes and in the end their effect on precipitation and mechanical properties. The model can be used to optimize PWHT for better controlling the final weld quality. The paper gives details of the model, with appropriate referencing and results for a specific case where hardness evaluation has been validated.

2. Numerical Models

2.1 Finite Element Model

A rotating tool is inserted into the centerline of the weld in a speed of 0.1 mm/s. In this plunging process, the material around the welding tool is preheated. Preheating is very important for FSW to avoid welding defects (Ref 54). The welding speed is 100 mm/min, and the rotating speed is 1000 rev/min. The diameter of the shoulder is 10 mm, and the pin diameter is 3 mm. The tilt angle is 2°. The material of the welding tool is H13 steel and is treated as a rigid body in the finite element model. The welded plate becomes 50 mm × 80 mm × 3 mm. The material of the welding plate is AA6005 initially in peak-aged state. The finite element model of the welding plate consists initially of 22,423 elements. The flow stress of AA6005 is temperature dependent, as shown in Fig. 1. Due to the fact that the temperature fields can be accurately predicted even if the physical parameters are considered to be constant (Ref 55, 56), the physical parameters used in this model are also considered to be constant, as shown in Ref 22.

The temperature field can be obtained by solving the semi-discretized heat conduction equation,

$$C_T \dot{T} + K_T T = P_T, \qquad (Eq\ 1)$$

where C_T is the heat capacity matrix, K_T is the thermal conductivity matrix, T is temperature, and P_T is the heat flux vector. This FE formulation for calculating the new temperature can be found by the finite difference approximation as follows (Ref 57):

$$T_{t+\Delta t} = T_t + \Delta t[(1 - \beta)T_{\Delta t} + \beta T_{t+\Delta t}], \qquad (Eq\ 2)$$

where β is the parameter controlling the convergence of the time and is selected to be 0.75.
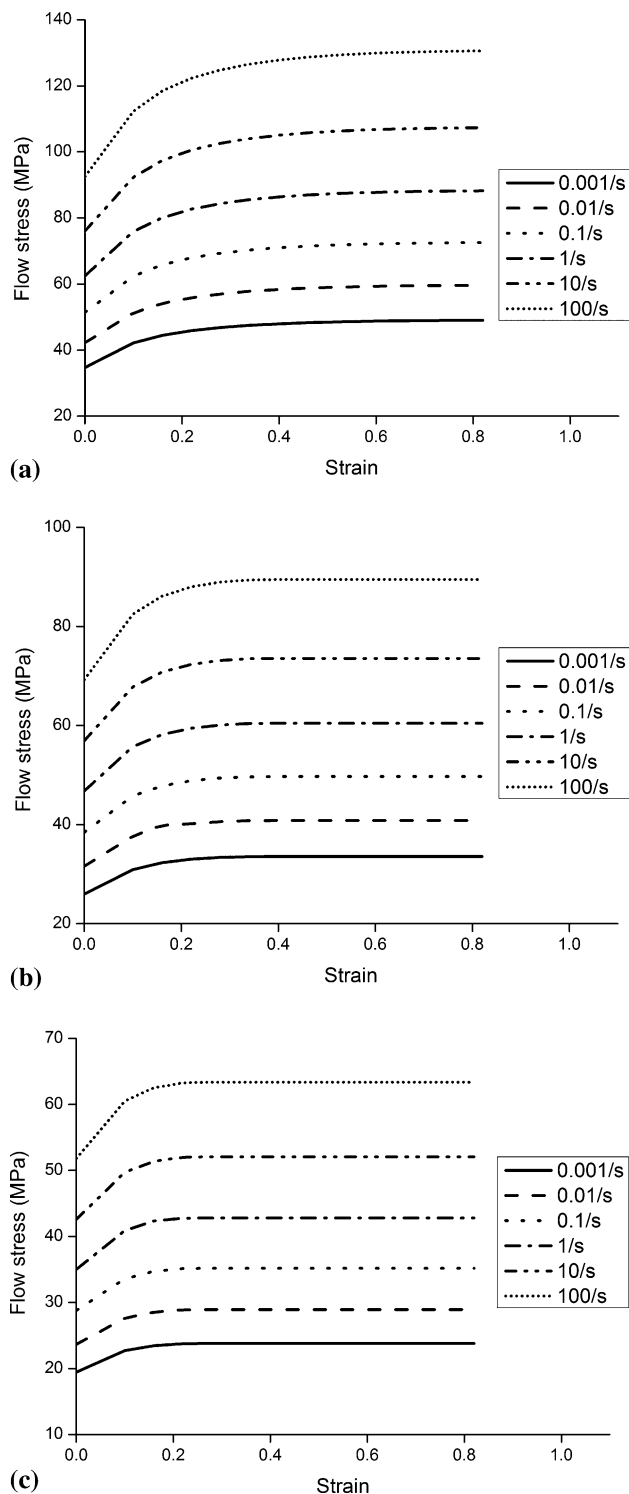

Fig. 1 Flow stress of Al-Mg-Si alloy. (a) 300 (b) 400 (c) 500 °C

The solution procedure of the mechanical response is based on the assumption of quasi-static conditions. The semi-discretized equilibrium equations are

$$F_{\text{int}} = F_{\text{ext}}(t), \tag{Eq 3}$$

where F_{int} is the vector of internal forces due to stresses and F_{ext} is the vector due to the applied thermal and mechanical loads. Utilizing a conjugate gradient iterative solution procedure leads to,

$$_i K_i \Delta U = {}_i^{n+1} F_{\text{ext}}(t), \tag{Eq 4}$$

where K is the tangent stiffness matrix and ΔU is the incremental displacements. Strains and stresses are subsequently computed from the obtained displacements.

The solution of these fields is updated at the end of each time increment and then mapped onto a new generated mesh. Detailed information on re-meshing technique can be found in Ref 58, 59. Re-meshing is used to avoid mesh distortions and entanglements. This is very important for the successful simulation of the FSW process. Deform 3D is used to simulate the friction stir welding process. Traced particles are used to track the material flows in the FSW process, and then the thermal histories of these traced particles are extracted for further calculations on microstructural evolutions. This method has been successfully used to simulate the grain growth in FSW (Ref 33). FORTRAN code is compiled for calculations of the precipitates and mechanical properties of the friction stir welds.

2.2 Heat Generation

In FSW, the heat is generated by both friction and plastic deformation (Ref 56). The frictional generated heat due to the contact between the pin and the plate material on a node is given by

$$p_i = \delta \cdot f_i \cdot \dot{\gamma}_i, \tag{Eq 5}$$

where f_i is the friction force on a node tangential to the contact. It is obtained from the contact algorithm, where it is computed from the used friction model. δ determines the amount of frictional work that becomes heat and is chosen as 0.9 (Ref 60). $\dot{\gamma}$ is the relative velocity between the contact surfaces. The relative sliding velocity is obtained from,

$$\dot{\gamma} = v_{\text{tool}} - v_{\text{plate}}, \tag{Eq 6}$$

where $\dot{\gamma}$ is evaluated at the contact point. The nodal power p_i is assembled to P_T in Eq 1 for all nodes that are in sliding contact.

The heat due to plastic dissipation in an integration point of an element is,

$$D_{\text{pl}} = \eta \sigma : \dot{\varepsilon}^{\text{p}}, \tag{Eq 7}$$

where η represents the inelastic heat fraction, which is selected to be 0.9 by default, σ is the stress tensor, and $\dot{\varepsilon}^{\text{p}}$ is the corresponding tensor of plastic strain rate. The plastic dissipated energy is integrated over an element and distributed to its nodes and then assembled to P_T in Eq 1. The flow stress is tabulated in a multi-dimensional table where it is a function of plastic strain, its rate, and temperature (Ref 60),

$$\sigma_y = \sigma_y(\bar{\varepsilon}^{\text{p}}, \ \dot{\bar{\varepsilon}}^{\text{p}}, \ T). \tag{Eq 8}$$

2.3 Precipitation Evolution Model and Flow Stress Model

The precipitation evolution model (Ref 61, 62) is combined with the above-mentioned re-meshing model to simulate the precipitation evolutions in FSW and calculate the mechanical properties in FSW with different post-weld heat treatments. The formation of the precipitates in Al-Mg-Si alloy consists of the nucleation and the coarsening processes. Kampmann–Wagner numerical model is used for calculation of precipitate evolutions. With the calculated precipitation, the yield strength of the weld can be computed. The yield strength of the friction stir weld can be divided into three parts,

$$\sigma_y = \sigma_0 + \sigma_{\text{ss}} + \sigma_{\text{preci}}, \tag{Eq 9}$$

where σ_0 is the intrinsic yield strength of pure aluminum, σ_{ss} is the additional contribution from solid solution, and σ_{preci} from precipitates.

The solid solution contribution to the flow stress (Ref 62) is computed by,

$$\sigma_{\text{ss}} = \sum_{i=1}^{3} k_i C_i^{2/3}, \tag{Eq 10}$$

where k_i is the scaling factor for alloying element i and C_i is its concentration. The solute elements for solid solution are Mg, Si, and Cu, indexed $i = 1$, 2, and 3. $k_1 = 66.3$ (MPa/wt.%$^{2/3}$), $k_2 = 29$ (MPa/wt.%$^{2/3}$), and $k_3 = 46.4$ (MPa/wt.%$^{2/3}$) (Ref 62).

The precipitate contribution to the flow stress is given by,

$$\sigma_{\text{preci}} = \frac{M\bar{F}}{b\bar{L}}, \tag{Eq 11}$$

where M is the Taylor factor, b is the Burgers vector, and $\bar{L}$ is mean particle spacing along the dislocation line. $\bar{F}$ is the mean obstacle strength, expressed as,

$$\bar{F} = \frac{\sum_i N_i(r)F_i(r)}{\sum_j N_j(r)}, \tag{Eq 12}$$

where $F_i(r)$ is the obstacle strength of a given discretized class. It is a function of the particle radius r_i. Small particles are sheared, particle cutting, by dislocations, whereas they bow around large precipitates. There is a critical radius r_c separating these two regions. The strength of small particles is proportional to their radius (Ref 62),

$$F_i = 2\beta Gb^2 \left(r_i / r_c \right). \tag{Eq 13}$$

Strong particles, characterized by $r_i > r_c$, are assumed to have a constant strength that is (Ref 62),

$$F_i = 2\beta Gb^2, \tag{Eq 14}$$

where β is the dislocation tension factor taken as 0.36 and G is the shear modulus of aluminum matrix, which is 2.7×10^{10} Pa.

Meanwhile, the mean particle spacing $\bar{L}$ along the dislocation line can be replaced by a function of mean particle radius $\bar{r}$ according to Ref 62. Then, Eq 11 can become,

$$\sigma_{\text{preci}} = \frac{M}{b\bar{r}} \left(2\beta Gb^2 \right)^{-\frac{1}{2}} \left(\frac{3f}{2\pi} \right)^{\frac{1}{2}} \bar{F}^{\frac{3}{2}} \tag{Eq 15}$$

3. Results and Discussions

The precipitate model is validated by comparing measurements from Myhr et al. (Ref 62) with simulations for the
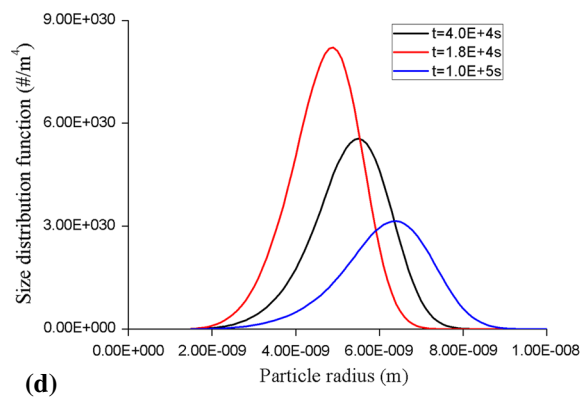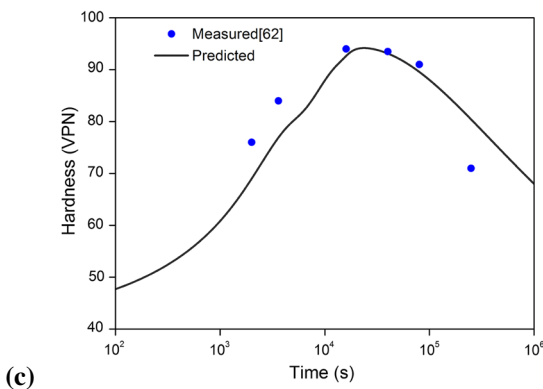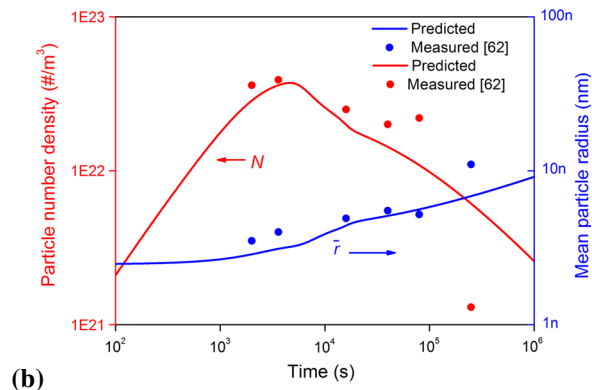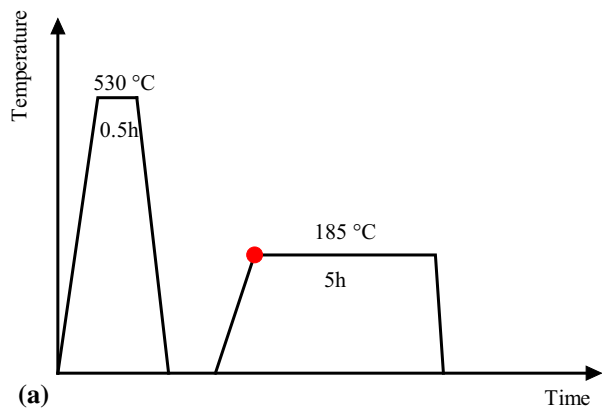
(a)

(b)

(c)

(d)

Fig. 2 Precipitation evolution in isothermal heat treatment. (a) Temperature history, (b) comparisons of particle number density and mean radius, (c) comparison of hardness, (d) size distribution function

isothermal (185 °C) heat treatment of precipitates in Fig. 2. It also includes measured and computed hardness changes. The used temperature curve is shown in Fig. 2(a). The number density and the average sizes agree well with measurements, as shown in Fig. 2(b). Hardness, as well as the yield strength, is one of the most important mechanical properties for welded material. Linear relation can be found between the flow stress and the hardness (Ref 63). The yield strength and the tensile strength can be treated as the start and end points of linear curve of the calculated flow stress. The linear relation is also clearly observed in experimental tests (Ref 63, 64). Then, a linear relation between the hardness and the flow stress can be obtained (Ref 65),

$$HV = 0.33\ \sigma_y + 16. \tag{Eq 16}$$

The flow stress is obtained from Eq 9, which includes the effect of precipitates. Predicted hardness and measured hardness are shown in Fig. 2(c). When the precipitate density starts to grow, the hardness of the material is increased. When the precipitate density reaches its maximum and then starts to decrease, the hardness has not reached its maximum and is still increasing. In current stage, smaller precipitates are dissolved and bigger precipitates grow, as shown in Fig. 2(d). Figure 2(d) shows computed size distributions discretized into about 1000 size classes (0.01 nm is selected as the interval size). Most of the precipitate radii are still smaller than the critical radius. The strength of material is governed by Eq 13. This is the reason that the hardness can be still increased in current stage. When the precipitates further grow, the mean radius is obviously bigger than the critical radius. The strength of the material is then governed by Eq 14, which can lead to the obvious hardness decrease.

Figure 3 shows the comparison between the calculated values and the corresponding numerical and experimental results in FSW for further validations. Figure 3(a) shows the used temperature curves. With consideration of the temperature curves, the precipitate radii and the volume fraction of precipitates can be calculated by use of the compiled code. The volume fraction and the mean radius of the precipitates are compared with the numerical results from Ref 36 with the same temperature input in the compiled code. The comparison shows the current code is very successful. Then, the hardness can be calculated by use of the Eq 16. The calculated hardness by current code can be compared to the experimental data (Ref 36). In this experiment, Vickers 1 kg hardness test is performed on the transverse section. The comparison of the numerical and experimental results can be fitted well, which can further validate the current model.

By use of the finite element re-meshing model of FSW, the temperature distributions and histories can be obtained, as shown in Fig. 4. The validity of the model for prediction of temperatures in FSW has been shown in our previous work (Ref 66). The whole FSW process lasts for 135 s. The effective plastic strain distribution at the end of FSW is shown in Fig. 5. The evolution of precipitates and corresponding mechanical property changes at the location being 6 mm away from weld centerline is shown in Fig. 6. The precipitate evolution from solid solution to the initial state before welding is computed by an "artificial ageing" (AA) step with the temperature shown to left in Fig. 6(a). This gives the T6 state of AA6005 as the initial state. The temperature history shown to right in Fig. 6(a) is obtained from the FSW simulation at a point 6 mm away from
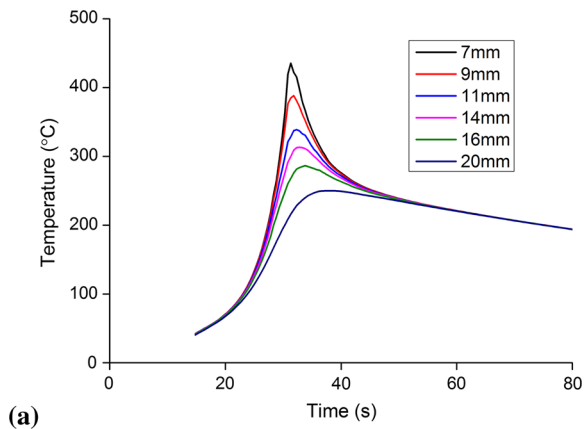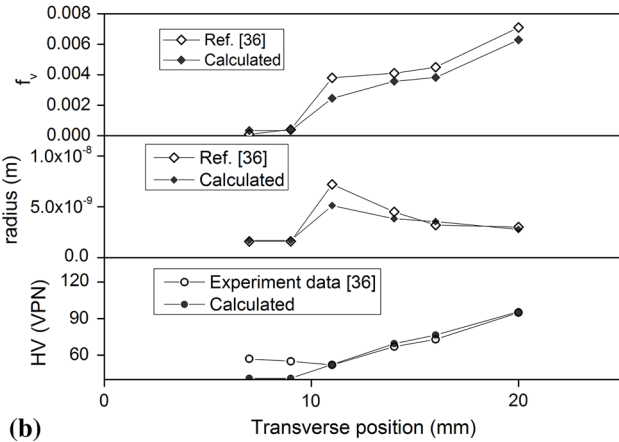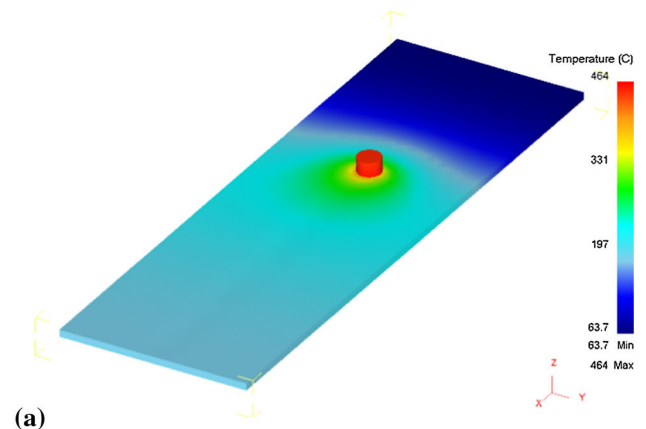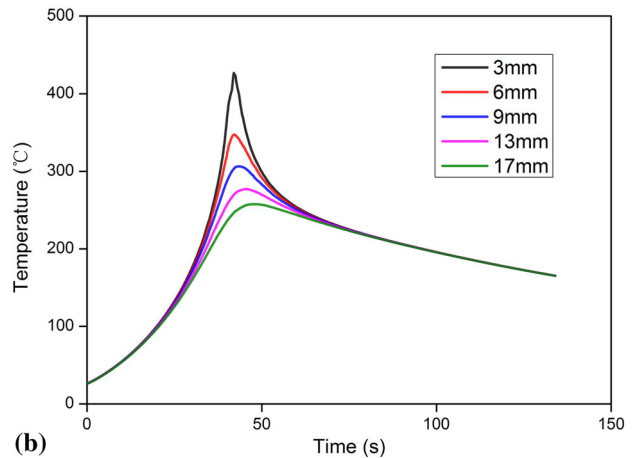
Fig. 3 Comparison between predicted values and numerical and experimental results. (a) Temperature curves used for validation, (b) comparisons of volume fraction, particle sizes, and hardness

Fig. 4 Predicted temperatures in FSW. (a) Temperature distribution, (b) temperature histories

the weld center line. The rate of nucleation of precipitates increases with temperature, as can be seen from Fig. 6(a) and (b). However, there is a reduction in this rate after some aging when the amount of precipitates has been increased. It can also be seen in Fig. 6(b) that the precipitate number density decreases with temperature due to the dissolution of the small particles. The dissolution can lead to a quick decrease in the volume fraction of precipitates. However, the coarsening that takes place gives much larger precipitates that maintain the volume fraction of precipitates to be constant, as shown in Fig. 6(c). This leads to a fairly constant flow stress, as shown in Fig. 6(d), despite of the dissolution of small precipitates.

The final computed precipitate distribution and hardness after welding for a cross section are shown in Fig. 7. The strengthening loss in the nugget zone for Al-Mg-Si is obvious. The volume fraction of precipitates after welding is about 0.04% in this zone according to Fig. 7(a). The volume fraction of precipitates is about 0.78% in the base metal. This shows that the decrease in volume fraction of precipitates is the main reason for reduced strength in the stirring zone, as shown in Fig. 7(b). It can be also seen that the precipitate sizes in the heat affected zone are larger than in the SZ and the base metal. Further increase in temperature can lead to a further increase in the precipitate sizes, i.e, more overaging, which can lead to even lower flow stress.
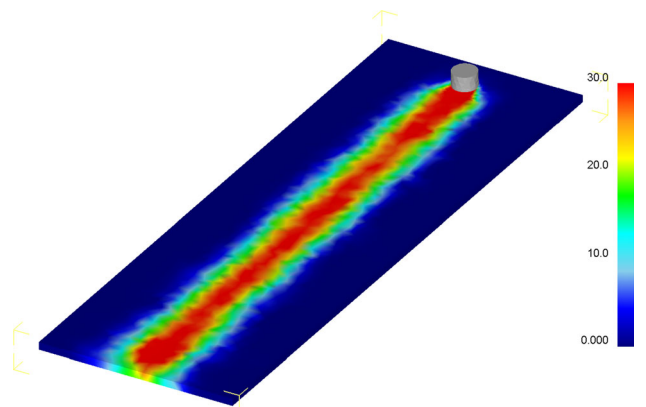

Fig. 5 Effective plastic strain

The effect of PWHT on mechanical properties of friction stir welding is shown in Fig. 8. Both the holding time and holding temperature can affect the final mechanical properties of friction stir weld. So, different cases, including 3, 5, and 8 h as holding times and 140, 160, 180, and 200 °C as holding temperatures, are investigated in detail. The hardness in the weld centerline is rising from 47VPN of as-welded state up to 64VPN, 65VPN, and 67VPN for holding times of 3, 5, and 8 h
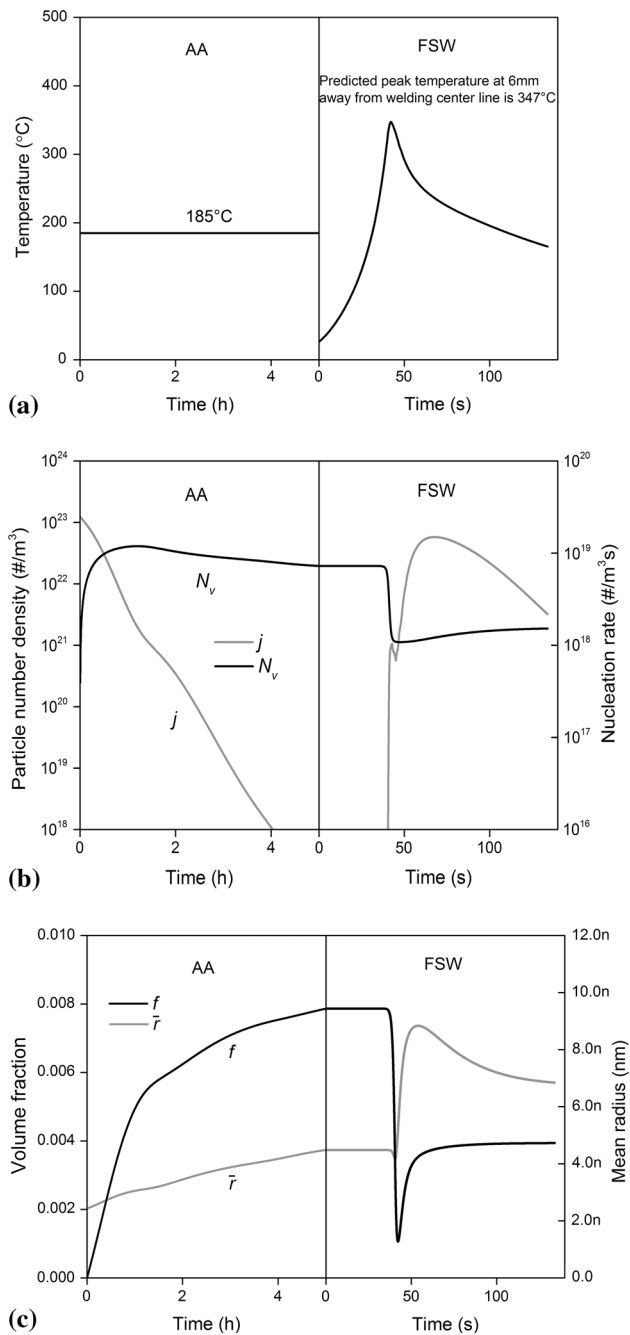
Fig. 6 continued

Fig. 6 Evolution of precipitates and mechanical properties at 6 mm from weld line. (a) Temperature curve, (b) particle density and nucleation rate, (c) volume fraction and mean radius, (d) yield strength and hardness

with holding temperature of 140 °C, respectively. When the PWHT holding temperature is increased to 160 °C with holding times of 3, 5, and 8 h, the hardness in SZ is increased to 71VPN, 76VPN, and 81VPN. When the PWHT holding temperature is further increased to 180 °C, the value in SZ is recovered up to 85.5VPN, 88.8VPN, and 89.4VPN. This is about 95% of the base metal for the holding time of 8 h. This recovery stems from the increase in the precipitate volume fraction in SZ. Increases in both the holding time and holding
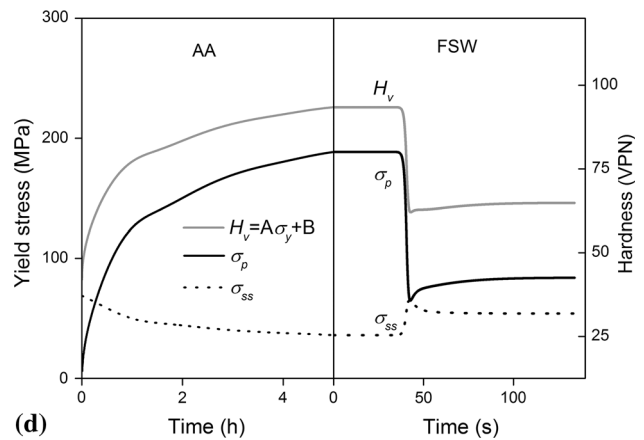
temperature can lead to the increase in the hardness in SZ when the holding temperature is not excessively high. The effect of holding time on recovery of mechanical property is not as strong as the holding temperature. A further increase in PWHT holding temperature to 200 °C does not give a corresponding improvement. For the PWHT holding temperature of 200 °C, hardness in SZ is recovered to 85.8VPN (3 h), 83.3VPN (5 h), and 80.5VPN (8 h). The increase in the holding time leads to a decrease in hardness in SZ. The precipitates grow quickly when the PWHT temperature is excessively high. Further increase in holding time will lead to a further increase in precipitate sizes. Thus, the PWHT holding time and temperature need to be selected with care. But it is also found from Fig. 8 that the mechanical property of HAZ is not obviously improved by PWHT.

To explain the variation of mechanical properties in SZ and HAZ, the volume fractions and the mean radii of the precipitate sizes are shown in Fig. 9 and 10. When the PWHT temperature is increased from 140 to 160 and 180 °C with holding time of 3 h, the volume fraction of precipitates in the weld centerline is increased from 0.1 to 0.3 and 0.67%. The mean radius of precipitate is increased from 3.1 to 3.2 nm and 4.1 nm. The increase of mechanical property stems from the increase of the volume fraction. For the case of holding time of 5 h shown in Fig. 9(b) and 10(b), the volume fractions are 0.19, 0.41, and 0.77%. The mean radii are 3, 3.3, and 4.8 nm. For the case of holding time of 8 h shown in Fig. 9(c) and 10(c), the volume fractions are 0.22, 0.56, and 0.83%. The mean radii are 2.9, 3.5, and 5.2 nm. When the holding temperature is increased from 140 to 160 and 180 °C with holding time of 3 h, the volume fractions of precipitates in HAZ are 0.4, 0.44, and 0.58%. Meanwhile, the mean radii of precipitates in HAZ are 6.6, 6.3, and 6.9 nm. When the holding time is 5 h, the mean radii of precipitates in HAZ are 6.45 nm (140 °C), 6.16 nm (160 °C), and 7.31 nm (180 °C). The corresponding volume fractions are 0.41, 0.47, and 0.68%. When the holding time is up to 8 h, the mean radii of precipitates in HAZ are 6.27 nm (140 °C), 6.08 nm (160 °C), and 7.82 nm (180 °C) and the volume fractions are 0.42, 0.51, and 0.77%. With the analysis of variation changes in hardness shown in Fig. 8, it can be concluded that in HAZ, the mean radii are nearly double than the ones in SZ with smaller volume fractions. So the obvious
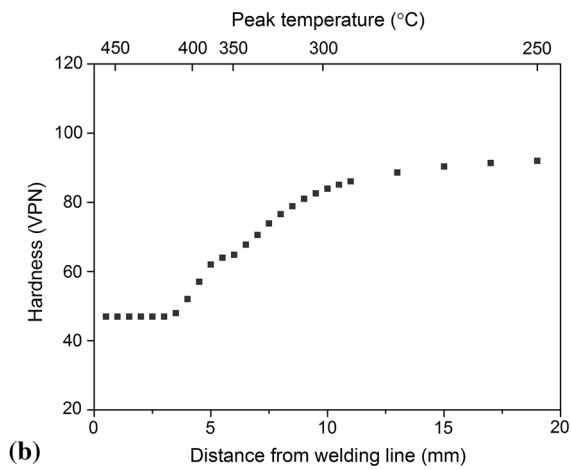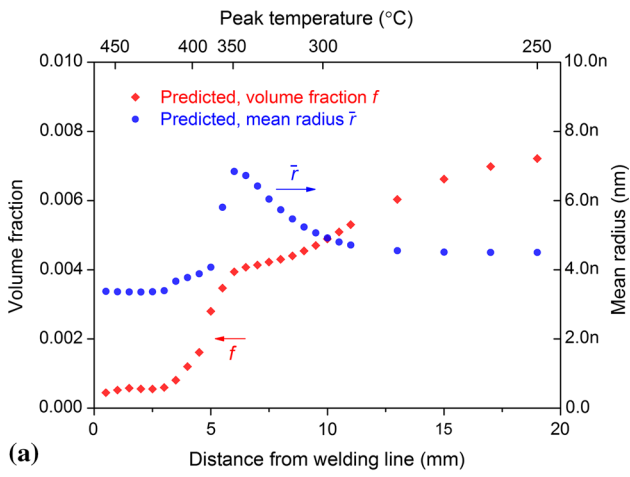
Fig. 7 Precipitates and mechanical properties in as-weld state. (a) Volume fraction and mean radius, (b) hardness

coarsening phenomenon in HAZ is the main reason for the fact that the mechanical property inside HAZ cannot be recovered by PWHT.

When the PWHT holding temperature is excessively high (e.g. 200 °C), the volume fraction of precipitates in SZ only rises from 0.84 to 0.86% (2.4% increase) when the holding time is increased from 3 to 8 h. But at the same time, the precipitate mean radius is increased from 5.8 to 6.7 nm (15.5% increase). The increase in mean radii of precipitates is more obvious than volume fraction. This can be the reason for the decrease of mechanical properties with longer holding time when the holding temperature is excessively high. So, the holding temperature needs to be carefully controlled for better mechanical property inside SZ in FSW.

To reveal the precipitate size distributions, Fig. 11 shows the precipitate sizes along radius direction in FSW with PWHT (3 h and 160 °C). In SZ, the mean radii are mainly focused on smaller sizes around 2.5 nm. But in HAZ, the larger precipitates around 10 nm are obviously increased. This means that the coarsening of precipitates in HAZ are the main reason to
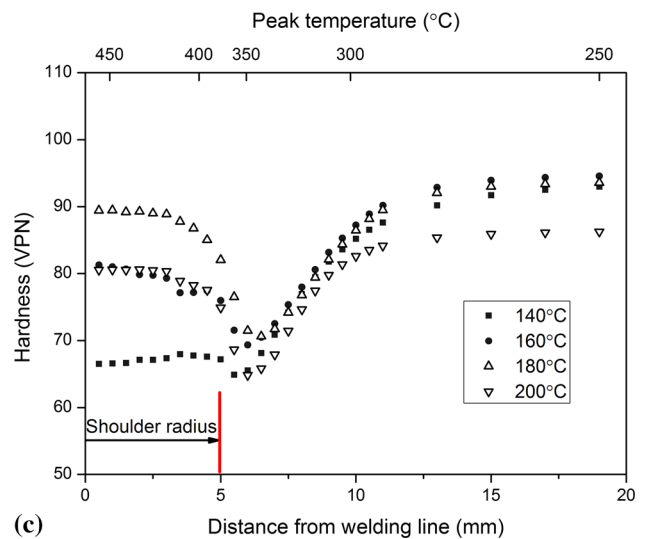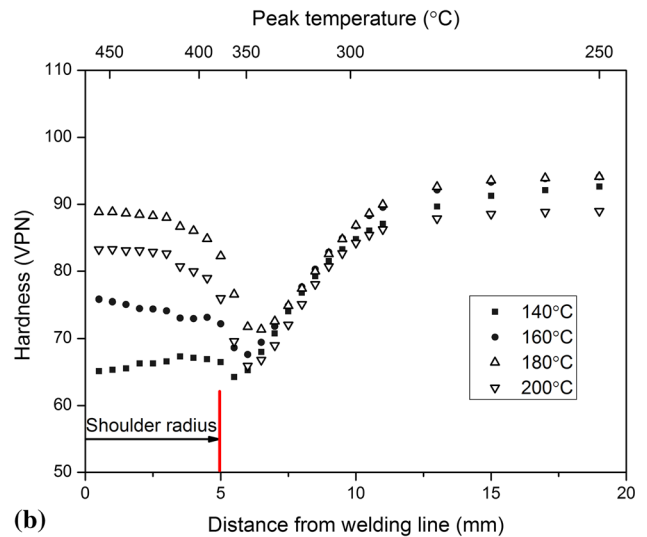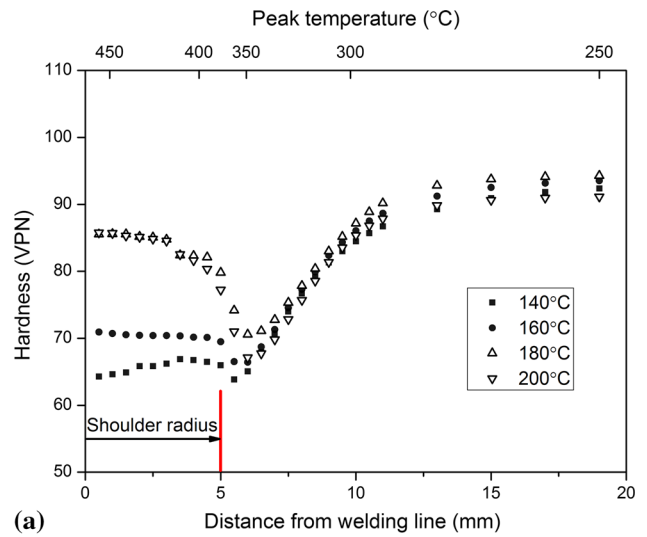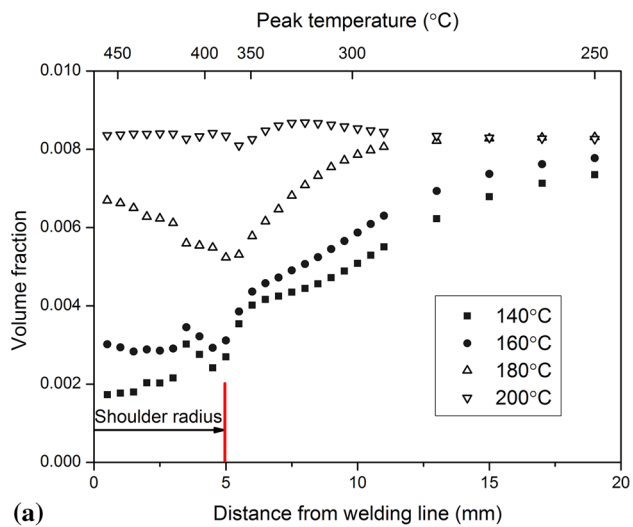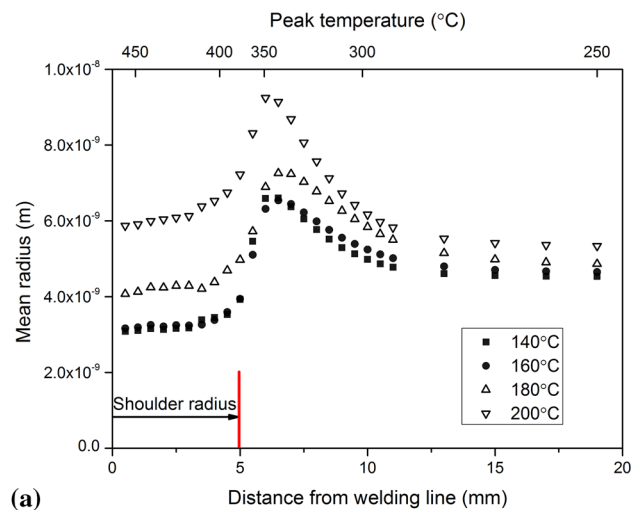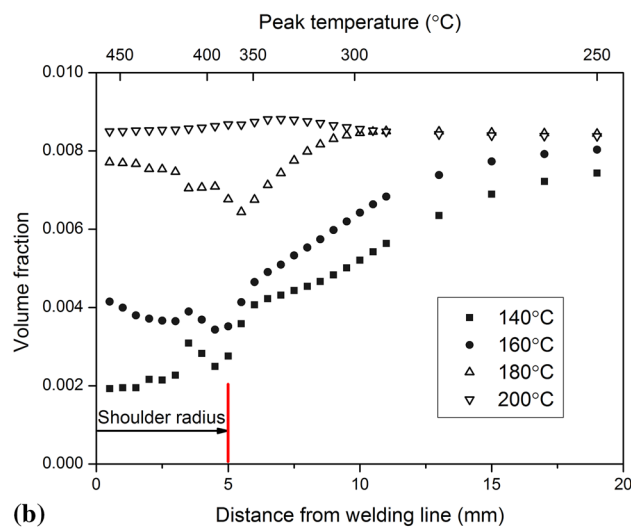

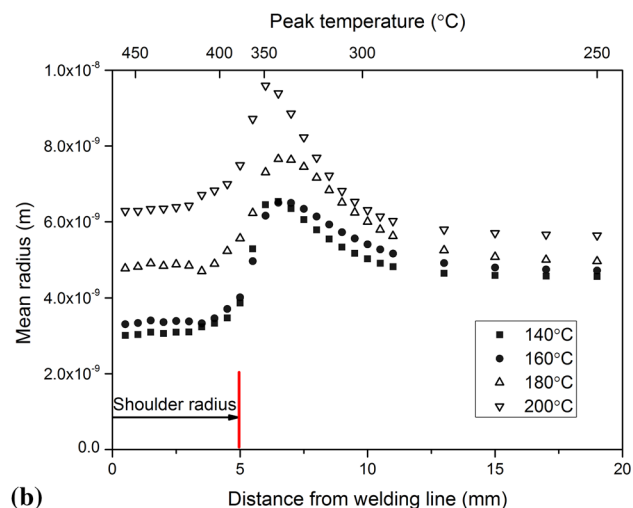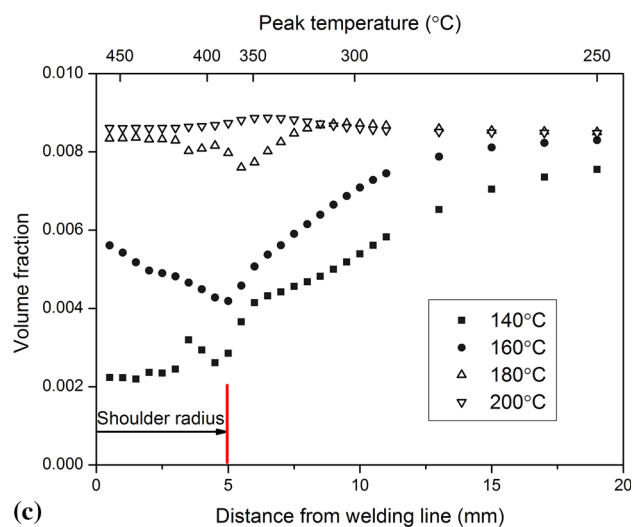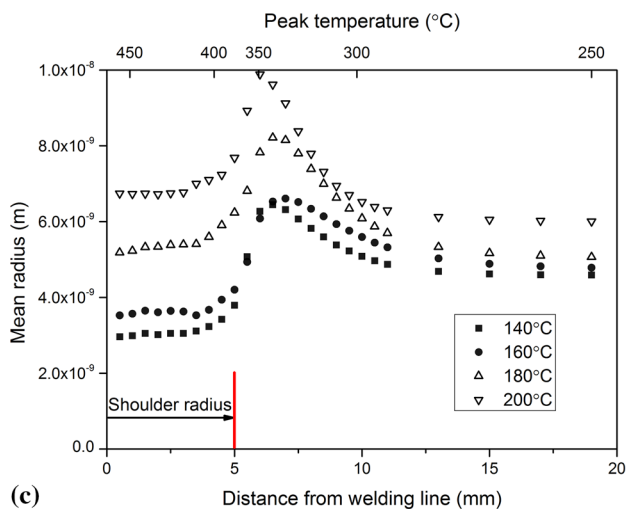**Fig. 8** Effect of PWHT on mechanical properties. (a) 3, (b) 5, (c) 8 h

Fig. 9 Effect of PWHT on volume fraction of precipitate. (a) 3, (b) 5, (c) 8 h

Fig. 10 Effect of PWHT on mean radius of precipitate. (a) 3, (b) 5, (c) 8 h
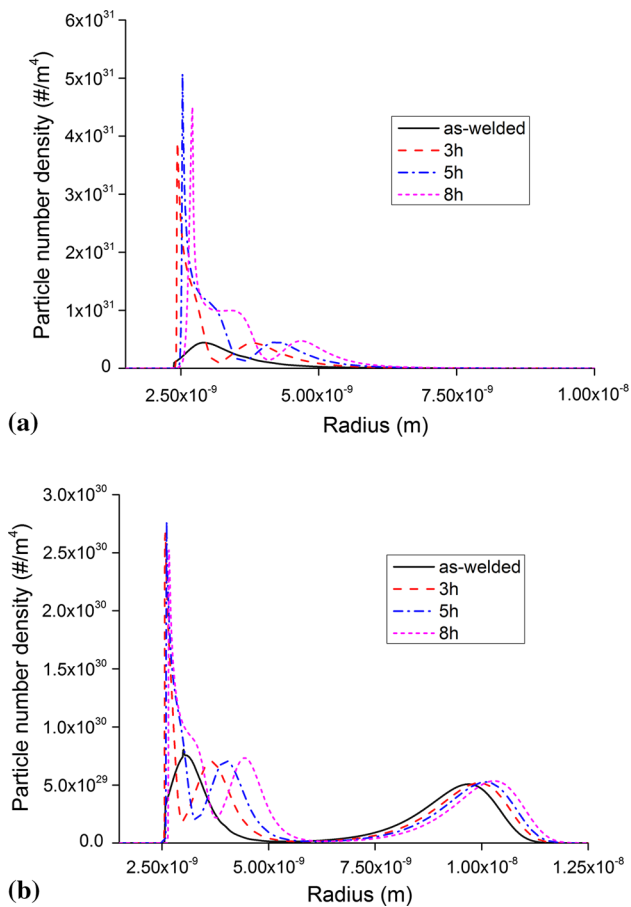
Fig. 11 Precipitate size distributions. (a) SZ, (b) HAZ

hinder the improvement of mechanical property when PWHT is used.

4. Conclusions

A precipitate evolution model is coupled with the FSW process model and the subsequent PWHT model. The effects of PWHT on mechanical properties of friction stir weld have been studied in detail. The main conclusions are the following:

1. The larger precipitates are growing but the smaller precipitates are dissolving in the PWHT process. The changes in mean radius and volume fractions during this process control the variations of mechanical properties in FSW.
2. Both the volume fractions and the sizes of precipitates can be increased with PWHT. A higher precipitate number with relatively smaller precipitate sizes leads to an increase of mechanical properties. This is the reason that the mechanical properties in the stirring zone can be recovered.
3. In comparison with the stirring zone, the coarsening of precipitates in HAZ is the main reason that the mechanical properties cannot be directly improved by PWHT.

Conflict of Interest

The authors declare that they have no conflict of interest.

References

1. D. Lohwasser and Z. Chen, *Friction Stir Welding: From Basics to Applications*, Woodhead Publishing, Sawston, 2010
2. F.F. Wang, W.Y. Li, J. Shen, Z.H. Zhang, J.L. Li, and J.F. dos Santos, Global and Local Mechanical Properties and Microstructure of Bobbin Tool Friction-Stir-Welded Al-Li Alloy, *Sci. Technol. Weld. Joining*, 2016, **21**, p 479–483
3. P.L. Threadgill, A.J. Leonard, H.R. Shercliff, and P.J. Withers, Friction Stir Welding of Aluminium Alloys, *Int. Mater. Rev.*, 2009, **54**, p 49–53
4. L. Commin, M. Dumont, J.E. Masse, and L. Barrallier, Friction Stir Welding of AZ31 Magnesium Alloy Rolled Sheets: Influence of Processing Parameters, *Acta Mater.*, 2009, **57**, p 326–334
5. S. Palanivel, A. Arora, K.J. Doherty, and R.S. Mishra, A Framework for Shear Driven Dissolution of Thermally Stable Particles During Friction Stir Welding and Processing, *Mater. Sci. Eng. A*, 2016, **678**, p 308–314
6. S. Mironov, T. Onuma, Y.S. Sato, S. Yoneyama, and H. Kokawa, Tensile Behavior of Friction-Stir Welded AZ31 Magnesium Alloy, *Mater. Sci. Eng. A*, 2017, **679**, p 272–281
7. S. Yoon, R. Ueji, and H. Fujii, Effect of Rotation Rate on Microstructure and Texture Evolution During Friction Stir Welding of Ti-6Al-4 V Plates, *Mater. Charact.*, 2015, **106**, p 352–358
8. L.H. Wu, B.L. Xiao, D.R. Ni, Z.Y. Ma, X.H. Li, M.J. Fu, and Y.S. Zeng, Achieving Superior Superplasticity from Lamellar Microstructure of a Nugget in a Friction-Stir-Welded Ti-6Al-4 V Joint, *Scr. Mater.*, 2015, **98**, p 44–47
9. J.J. Shen, H.J. Liu, and F. Cui, Effect of Welding Speed on Microstructure and Mechanical Properties of Friction Stir Welded Copper, *Mater. Des.*, 2010, **31**, p 3937–3942
10. T. Sakthivel and J. Mukhopadhyay, Microstructure and Mechanical Properties of Friction Stir Welded Copper, *J. Mater. Sci.*, 2007, **42**, p 8126–8129
11. A. De, H.K.D.H. Bhadeshia, and T. DebRoy, Friction Stir Welding of Mild Steel: Tool Durability and Steel Microstructure, *Mater. Sci. Technol.*, 2014, **30**, p 1050–1056
12. MdM Husain, R. Sarkar, T.K. Pal, N. Prabhu, and M. Ghosh, Friction Stir Welding of Steel: Heat Input, Microstructure, and Mechanical Property Co-relation, *J. Mater. Eng. Perform.*, 2015, **24**, p 3673–3683
13. H. Fujii, L. Cui, N. Tsuji, M. Maeda, K. Nakat, and K. Nogi, Friction Stir Welding of Carbon Steels, *Mater. Sci. Eng., A*, 2006, **429**, p 50–57
14. M.B. Prime, T. Gnäupel-Herold, J.A. Baumann, R.J. Lederich, D.M. Bowden, and R.J. Sebring, Residual Stress Measurements in a Thick, Dissimilar Aluminum Alloy Friction Stir Weld, *Acta Mater.*, 2006, **54**, p 4013–4021
15. W.B. Lee, Y.M. Yeon, and S.B. Jung, The Joint Properties of Dissimilar Formed Al Alloys by Friction Stir Welding According to the Fixed Location of Materials, *Scr. Mater.*, 2003, **49**, p 423–428
16. U. Donatus, G.E. Thompson, and X. Zhou, Effect of Prior Sputter Deposition of Pure Aluminium on the Corrosion Behaviour of Anodized Friction Stir Weld of Dissimilar Aluminium Alloys, *Scr. Mater.*, 2016, **123**, p 126–129
17. R. Nandan, T. DebRoy, and H.K.D.H. Bhadeshia, Recent Advances in Friction-Stir Welding—Process, Weldment Structure and Properties, *Prog. Mater Sci.*, 2008, **53**, p 980–1023

18. X.C. He, F.S. Gu, and A. Ball, A Review of Numerical Analysis of Friction Stir Welding, *Prog. Mater Sci.*, 2014, **65**, p 1–66

19. R.S. Mishra, M.W. Mahoney, S.X. McFadden, N.A. Mara, and A.K. Mukherjee, High Strain Rate Superplasticity in a Friction Stir Processed 7075 Al Alloy, *Scr. Mater.*, 1999, **42**, p 163–168

20. Z.Y. Ma, R.S. Mishra, and M.W. Mahoney, Superplastic Deformation Behaviour of Friction Stir Processed 7075Al Alloy, *Acta Mater*, 2002, **50**, p 4419–4430

21. Z. Zhang and Q. Wu, Numerical Studies of Tool Diameter on Strain Rates, Temperature Rises and Grain Sizes in Friction Stir Welding, *J. Mech. Sci. Technol.*, 2015, **29**, p 4121–4128

22. H. Schmidt and J. Hattel, A Local Model for the Thermomechanical Conditions in Friction Stir Welding, *Model. Simul. Mater. Sci. Eng.*, 2005, **13**, p 77–93

23. A. Gerlich, G. Avramovic-Cingara, and T.H. North, Stir Zone Microstructure and Strain Rate During Al 7075-T6 Friction Stir Spot Welding, *Metal. Mater. Trans. A*, 2006, **37**, p 2773–2786

24. M. Ghosh, K. Kumar, and R.S. Mishra, Analysis of Microstructural Evolution During Friction Stir Welding of Ultrahigh-Strength Steel, *Scr. Mater.*, 2010, **63**, p 851–854

25. S. Sabooni, F. Karimzadeh, M.H. Enayati, A.H.W. Ngan, and H. Jabbari, Gas Tungsten Arc Welding and Friction Stir Welding of Ultrafine Grained AISI, 304L Stainless Steel: Microstructural and Mechanical Behavior Characterization, *Mater. Charact.*, 2015, **109**, p 138–151

26. J.Y. Sheikh-Ahmad, F. Ozturk, F. Jarrar, and Z. Evis, Thermal History and Microstructure During Friction Stir Welding of Al-Mg Alloy, *Int. J. Adv. Manuf. Technol.*, 2016, **86**, p 1071–1081

27. J.S. Liao, N. Yamamoto, and K. Nakata, Effect of Dispersed Intermetallic Particles on Microstructural Evolution in the Friction Stir Weld of a Fine-Grained Magnesium Alloy, *Metal. Mater. Trans. A*, 2009, **40**, p 2212–2219

28. Z. Yang, S. Sista, J.W. Elmer, and T. DebRoy, Three Dimensional Monte Carlo Simulation of Grain Growth During GTA Welding of Titanium, *Acta Mater.*, 2000, **48**, p 4813–4825

29. S. Sista, Z. Yang, and T. DebRoy, Three-Dimensional Monte Carlo Simulation of Grain Growth in the Heat-Affected Zone of a 2.25Cr-1Mo Steel Weld, *Metal. Mater. Trans. B*, 2000, **31**, p 529–536

30. S. Sista and T. DebRoy, Three-Dimensional Monte Carlo Simulation of Grain Growth in Zone-Refined Iron, *Metal. Mater. Trans. B*, 2001, **32**, p 1195–1201

31. S. Mishra and T. DebRoy, Measurements and Monte Carlo Simulation of Grain Growth in the Heat-Affected Zone of Ti-6Al-4 V Welds, *Acta Mater.*, 2004, **52**, p 1183–1192

32. Q. Wu and Z. Zhang, Precipitation Induced Grain Growth Simulation in Friction Stir Welding, *J. Mater. Eng. Perform.*, 2017, **26**(5), p 2179–2189

33. Z. Zhang, Q. Wu, M. Grujicic, and Z.Y. Wan, Monte Carlo Simulation of Grain Growth and Welding Zones in Friction Stir Welding of AA6082-T6, *J. Mater. Sci.*, 2016, **51**, p 1882–1895

34. M. Grujicic, S. Ramaswami, J.S. Snipes, V. Avuthu, R. Galgalikar, and Z. Zhang, Prediction of the Grain-Microstructure Evolution Within a Friction Stir Welding (FSW) Joint Via the Use of the Monte Carlo Simulation Method, *J. Mater. Eng. Perform.*, 2015, **24**, p 3471–3486

35. Z.Y. Wan, Z. Zhang, and X. Zhou, Finite Element Modelling of Grain Growth by Point Tracking Method in Friction Stir Welding of AA6082-T6, *Int. J. Adv. Manuf. Technol.*, 2017, **90**(9), p 3567–3574

36. A. Simar, Y. Bréchet, B. de Meester, A. Denquin, and T. Pardoen, Sequential Modeling of Local Precipitation, Strength and Strain Hardening in Friction Stir Welds of an Aluminum Alloy 6005A-T6, *Acta Mater.*, 2007, **55**, p 6133–6143

37. C. Genevois, A. Deschamps, A. Denquin, and B. Doisneau-cottignies, Quantitative Investigation of Precipitation and Mechanical Behaviour for AA2024 Friction Stir Welds, *Acta Mater.*, 2005, **53**, p 2447–2458

38. H.R. Shercliff and M.F. Ashby, A Process Model for Age Hardening of Aluminium Alloys, *Acta Metall. Mater.*, 1990, **38**(10), p 1789–1812

39. O.R. Myhr and Ø. Grong, Process Modelling Applied to 6082-T6 Aluminium Weldments, *Acta Metall. Mater.*, 1991, **39**, p 2693–2708

40. H.R. Shercliff, M.J. Russell, A. Taylor, and T.L. Dickson, Microstructural Modelling in Friction Stir Welding of 2000 Series Aluminium Alloys, *Mec. Ind.*, 2005, **6**, p 25–35

41. J.D. Robson, N. Kamp, and N.A. Sulliva, Microstructural Modelling for Friction Stir Welding of Aluminium Alloys, *Mater. Manuf. Process.*, 2007, **22**(4), p 450–456

42. O.R. Myhr and Ø. Grong, Modelling of Non-isothermal Transformations in Alloys Containing a Particle Distribution, *Acta Mater.*, 2000, **48**, p 1605–1615

43. R. Wagner and R. Kampmann, *Materials Science and Technology—A Comprehensive Treatment*, Wiley-VCH, Weinhem, 1991

44. L.-E. Lindgren, A. Lundbäck, and M. Fisk, Thermo-Mechanics and Microstructure Evolution in Manufacturing Simulations, *J. Therm. Stresses*, 2013, **36**(6), p 564–588

45. L.-E. Lindgren, A. Lundbäck, M. Fisk, R. Pederson, and J. Andersson, Simulation of Additive Manufacturing Using Coupled Constitutive and Microstructure Models, *Addit. Manuf.*, 2016, **12**, p 144–158

46. B. Lia, Y.F. Shen, L. Luo, and W.Y. Hu, Effects of Processing Variables and Heat Treatments on Al/Ti-6Al-4 V Interface Microstructure of Bimetal Clad-Plate Fabricated Via a Novel Route Employing Friction Stir Lap Welding, *J. Alloy. Compd.*, 2016, **658**, p 904–913

47. H. Sidhar and R.S. Mishra, Aging Kinetics of Friction Stir Welded Al-Cu-Li-Mg-Ag and Al-Cu-Li-Mg Alloys, *Mater. Des.*, 2016, **110**, p 60–71

48. M.N. Avettand-Fènoël and R. Taillard, Effect of a Pre or Postweld Heat Treatment on Microstructure and Mechanical Properties of an AA2050 Weld Obtained by SSFSW, *Mater. Des.*, 2016, **89**, p 348–361

49. R. Citarella, P. Carlone, M. Lepore, and R. Sepe, Hybrid Technique to Assess the Fatigue Performance of Multiple Cracked FSW Joints, *Eng. Fract. Mech.*, 2016, **162**, p 38–50

50. P. Carlone, R. Citarella, M.R. Sonne, and J.H. Hattel, Multiple Crack Growth Prediction in AA2024-T3 Friction Stir Welded Joints, Including Manufacturing Effects, *Int. J. Fatigue*, 2016, **90**, p 69–77

51. M.R. Sonne, C.C. Tutum, J.H. Hattel, A. Simar, and B.D. Meester, The Effect of Hardening Laws and Thermal Softening on Modeling Residual Stresses in FSW of Aluminum Alloy 2024-T3, *J. Mater. Process. Technol.*, 2013, **213**(3), p 477–486

52. Z. Zhang, P. Ge, and G.Z. Zhao, Numerical Studies of Post Weld Heat Treatment on Residual Stresses in Welded Impeller, *Int. J. Press. Vessels Pip.*, 2017, **153**, p 1–14

53. Z.W. Zhang, Z. Zhang, and H.W. Zhang, Effect of Residual Stress of Friction Stir Welding on Fatigue Life of AA 2024-T351 Joint, *Proceed. Inst. Mech. Eng. Part B J. Eng. Manuf.*, 2015, **229**(11), p 2021–2034

54. Z. Zhang and H.W. Zhang, Numerical Studies of Pre-Heating Time Effect on Temperature and Material Behaviors in Friction Stir Welding Process, *Sci. Technol. Weld. Joining*, 2007, **12**(5), p 436–448

55. Z. Zhang and J.T. Chen, Computational Investigations on Reliable Finite Element Based Thermo-Mechanical Coupled Simulations of Friction Stir Welding, *Int. J. Adv. Manuf. Technol.*, 2012, **60**, p 959–975

56. Z. Zhang and H.W. Zhang, Solid Mechanics-Based Eulerian Model of Friction Stir Welding, *Int. J. Adv. Manuf. Technol.*, 2014, **72**, p 1647–1653

57. G. Buffa, J. Hua, R. Shivpuri et al., A Continuum Based Fem Model for Friction Stir Welding—Model Development, *Mater. Sci. Eng. A*, 2006, **419**(1), p 389–396

58. O.C. Zienkiewicz, R.L. Taylor, and J.Z. Zhu, *Finite Element Method: Its Basis and Fundamentals*, 6th ed., Elsevier Pre Ltd, Singapore, 2008

59. O.C. Zienkiewicz and J.Z. Zhu, A Simple Error Estimator and Adaptive Procedure for Practical Engineering Analysis, *Int. J. Numer. Methods Eng.*, 1987, **24**(2), p 337–357

60. DEFORM 3D, *V6.1 User's Manual*, SFC, Columbus, 2007

61. D. Carron, P. Bastid, Y. Yin, and R.G. Faulkner, Modelling of Precipitation During Friction Stir Welding of an Al-Mg-Si Alloy, *Tech. Mech.*, 2010, **30**(1-3), p 29–44

62. O.R. Myhr, Ø. Grong, and S.J. Andersen, Modelling of the Age Hardening Behaviour of Al-Mg-Si Alloys, *Acta Mater.*, 2001, **49**(1), p 65–75

63. D. Umbrello, J. Hua, and R. Shivpuri, Hardness-Based Flow Stress and Fracture Models for Numerical Simulation of Hard Machining AISI, 52100 Bearing Steel, *Mater. Sci. Eng. A*, 2004, **374**, p 90–100

64. M.Y. He, G.R. Odette, T. Yamamoto, and D. Klingensmith, A Universal Relationship Between Indentation Hardness and Flow Stress, *J. Nucl. Mater.*, 2007, **367-370**, p 556–560

65. O.R. Myhr, Ø. Grong, H.G. Fjær, and C.D. Marioara, Modelling of the Microstructure and Strength Evolution in Al-Mg-Si Alloys During Multistage Thermal Processing, *Acta Mater.*, 2004, **52**, p 4997–5008

66. Z. Zhang and Z.Y. Wan, Predictions of Tool Forces in Friction Stir Welding of AZ91 Magnesium Alloy, *Sci. Technol. Weld. Join*, 2012, **17**(6), p 495–500